

<https://doi.org/10.1038/s41612-024-00754-7>

Predictability and prediction skill of summertime East/Japan Sea surface temperature events



Youngji Joh¹✉, SeonJu Lee^{2,3}, Young-Gyu Park², Thomas L. Delworth⁴, Gyundo Pak², Liwei Jia⁴, William F. Cooke⁴, Colleen McHugh^{4,5}, Young-Ho Kim⁶ & Hyung-Gyu Lim²

The East/Japan Sea (EJS), a marginal sea of the Northwestern Pacific, is one of the ocean regions showing the most rapid warming and greatest increases in ocean heatwaves over the last several decades. Predictability and skillful prediction of the summer season EJS variability are crucial, given the increasing severity of ocean temperature events impacting fisheries and reinforcing climate conditions like the East Asian rainy season, which in turn affects adjacent high-population density areas over East Asia. We use observations and the Geophysical Fluid Dynamics Laboratory (GFDL) Seamless System for Prediction and Earth System Research (SPEAR) seasonal forecast system to investigate the summertime EJS Sea Surface Temperature (SST) predictability and prediction skill. The observations and seasonal prediction system show that the summer season EJS SST can be closely linked to the previous winter air-sea coupling and predictable 8–9 months in advance. The SPEAR seasonal prediction system demonstrates skillful forecast of EJS SST events from summer to late fall, with added skill for long-lead forecasts initialized in winter. We find that winter large-scale atmospheric circulations linked to Barents Sea variability can induce persistent surface wind anomalies and corresponding northward Ekman heat transport over the East China Sea. The ocean advection anomalies that enter the EJS in prior seasons appear to play a role in developing anomalous SST during summer, along with instantaneous atmospheric forcing, as the source of long-lead predictability. Our findings provide potential applications of large-scale ocean-atmosphere interactions in understanding and predicting seasonal variability of East Asian marginal seas.

The summer of 2023 is reported as the world's warmest since global records began in late 1800¹. During July–September 2023, the Northern Hemisphere sea surface temperature (SST) field exhibited large warm anomalies spreading over broad regions of the Pacific and Atlantic Oceans with the developing warm phase of the El Niño–Southern Oscillation (ENSO) over the tropical Pacific (Fig. 1a). The Northwestern Pacific, which is adjacent to countries of large populations over East Asia, is one of the regions that experienced record-warmth in the summer of 2023². In particular, the East/Japan Sea (blue box in Fig. 1b), a marginal sea surrounded by the Korean Peninsula, Russia, and Japanese islands over the Northwestern Pacific, shows that the region has experienced consecutive record highs in recent years (i.e., 2021 to 2023; Fig. 1c). The linear trends of summer season SST

over the East/Japan sea (hereafter, EJS; 35°–45°N, 127°–142°E) exhibit exceptionally rapid warming rates compared to that of global SST^{3–12} as well as prominent seasonal SST variations (Fig. 1d). The strong seasonality and ocean warming of EJS SST variability can lead to more pronounced episodes linked to regional phenomena, such as the East Asian rainy season and heat extremes during summer, by providing heat and moisture to adjacent continents. Therefore, it is crucial to understand the underlying mechanisms and predictability of summer EJS SST variability and to assess and improve its prediction skills.

EJS ocean temperature events, including Marine Heatwaves (MHWs)^{13,14} have received increasing attention due to their strong seasonal characteristics^{4,5,9,15} as well as increasing intensity and more frequent MHW

¹Program in Atmospheric and Oceanic Sciences, Princeton University, Princeton, NJ, USA. ²Korea Institute of Ocean Science and Technology, Busan, South Korea. ³Cooperative Institute for Satellite Earth System Studies (CISESS)/Earth System Science Interdisciplinary Center (ESSIC), University of Maryland, College Park, MD, USA. ⁴Geophysical Fluid Dynamics Laboratory, NOAA/OAR, Princeton, NJ, USA. ⁵Science Applications International Corporation, Reston, VA, USA. ⁶Department of Oceanography, Pukyong National University, Busan, Republic of Korea. ✉e-mail: youngji.joh@princeton.edu

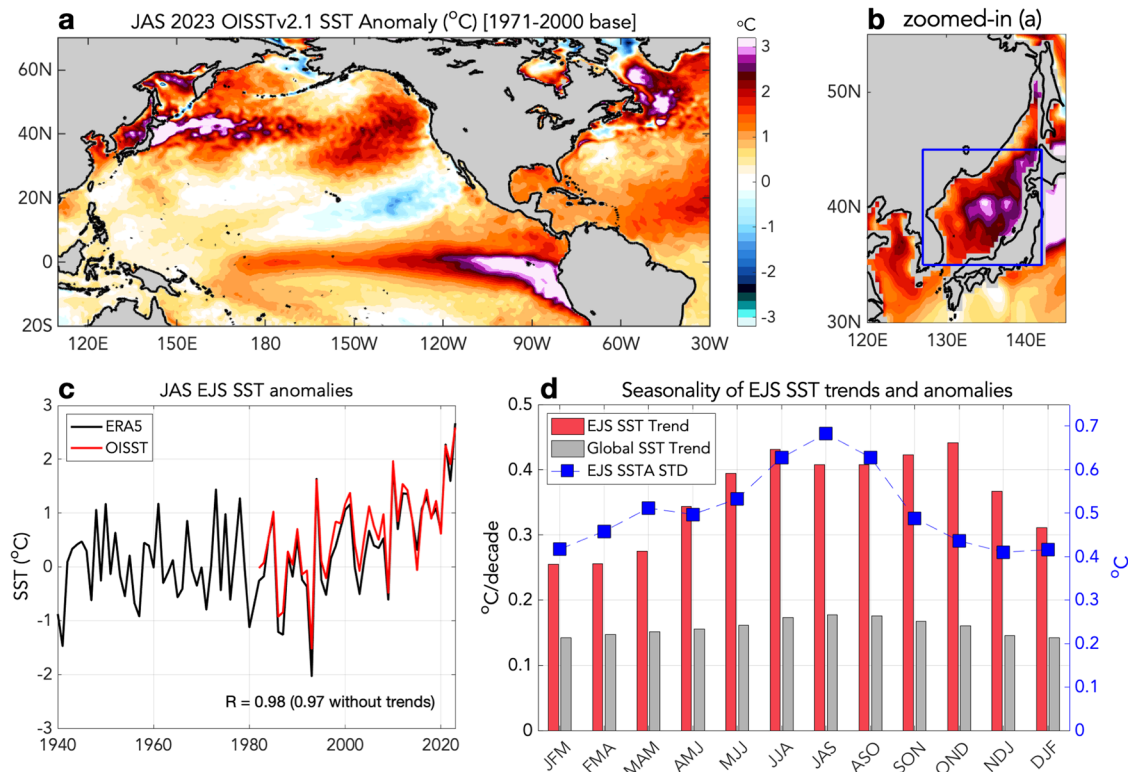


Fig. 1 | Seasonal Sea Surface Temperature (SST) variability and warming trends over the East/Japan Sea from the historical period. **a** 2023 Summer season (July–August–September) SST anomaly pattern, where the base period between 1971–2000 is used. **b** Zoomed-in section of (a), showing the East Asian Marginal seas, including the East/Japan Sea (EJS). The blue box denotes the region defined as the EJS region [35° – 45°N , 127° – 142°E] in the present study. **c** Temporal variations of the summer season EJS SST from the ERA5 (black) and OISST (red) data. **d** Linear

trends of seasonal SST anomalies averaged over the EJS (red bars) and global ocean (gray bars) and the variance of seasonal EJS SST anomalies (blue rectangles) using OISST (1982–2023). The left and right axis for trend and standard deviation, respectively. The long-term linear trend and climatological annual cycle are removed from each grid point when computing the standard deviation of seasonal EJS SST anomalies (blue rectangles).

events in a warming climate^{4,10,12}. Wang et al.¹⁰ have documented that the EJS MHW events show varying spatial distributions of warm anomalies depending on seasons. Specifically, in the cold season (e.g., winter to spring), EJS MHWs are especially prominent over the northwestern part of the EJS, while the summer season MHWs show homogeneous warming of the entire EJS. Focusing on the winter season EJS SST events, Song et al.¹⁵ use observations and reanalysis products and show that the wintertime MHW episodes over the northwestern EJS can be modulated by wind stress anomalies associated with Arctic Oscillation through ocean dynamic adjustment processes. Supportingly, Choi et al.⁹ have suggested that the winter EJS MHW events might be largely governed by regional oceanic processes, such as a northward shift of the subpolar front over the Northwestern Pacific.

Meanwhile, many studies^{4,7,9,10,16,17} have focused on the role of local and remote atmospheric forcing in driving summertime EJS MHWs. The recent findings show that an anomalous high-pressure atmospheric circulation, which indicates reduced cloud amount and increased solar radiation, is the most dominant driver of the summer season EJS warm SST events^{9,10,17}. In the context of large-scale climate variability, Lee et al.¹⁶ highlight the impacts of ENSO phase transitions and the subtropical convective forcing (e.g., Pacific–Japan pattern) in two dominant modes of summer East Asian MHWs. Oh et al.⁷ suggest the role of subtropical remote forcing in enhancing summer season EJS MHWs via persistent anticyclonic circulation with downward shortwave radiation and related oceanic responses. Another recent study points out that the longer duration and stronger intensity of summer MHWs over the East Asian marginal seas can be significantly attributed to changes in basin-scale ocean circulations (e.g., a northward shift of the East Korea Warm Current) and rapidly increasing mean SST⁴.

Given the suggested links to remote forcing^{7,10} and the significant duration of summer EJS SST anomalies that may lead to its predictable

variability, the present study aims to identify the potential source of summer EJS SST predictability and assess related forecast skills in the current seasonal forecast system. To explore physical mechanisms of summer EJS SST events and associated predictability and prediction skill, we use observations/reanalysis and Geophysical Fluid Dynamics Laboratory (GFDL) coupled climate modeling and prediction systems of SPEAR¹⁸ (Seamless system for Prediction and EArth system Research; see method for more details). In this study, we discuss potential connections between the seasonal EJS SST and large-scale air–sea coupled processes, as well as examine strategic improvements and limitations in summer season EJS SST prediction.

Results

Seasonal EJS SST anomalies and their linkages to large-scale patterns

Consistent with previous findings^{9,10}, we first confirm a distinct spatial structure of the EJS SST variability between summer (July–August–September, JAS) and winter (December–January–February, DJF) seasons in Fig. 2. The JAS EJS SST (Fig. 2a) exhibits the overall warming over the majority of the EJS basin, whereas that of DJF EJS SST (Fig. 2d) shows the SST signature confined to the local area, which is characterized by peak SST signals over the East Korean Bay. It is notable that both seasons' EJS SST patterns include large-scale anomalous SST over the North Pacific (Fig. 2b, e). While previous studies address potential impacts of the tropical Pacific (e.g., ENSO) in the East Asian marginal seas¹⁶, Fig. 2b and e reveal that the sole EJS variability might not be significantly associated with tropical Pacific SST anomalies in both summer and winter seasons. Supportingly, Fig. 2c and f indicate that the seasonal EJS SST variability is statistically independent of ENSO, exhibiting no significant correlations, where the Nino3.4 [5°S – 5°N , 170° – 120°E] SST anomalies lead the summer EJS SST

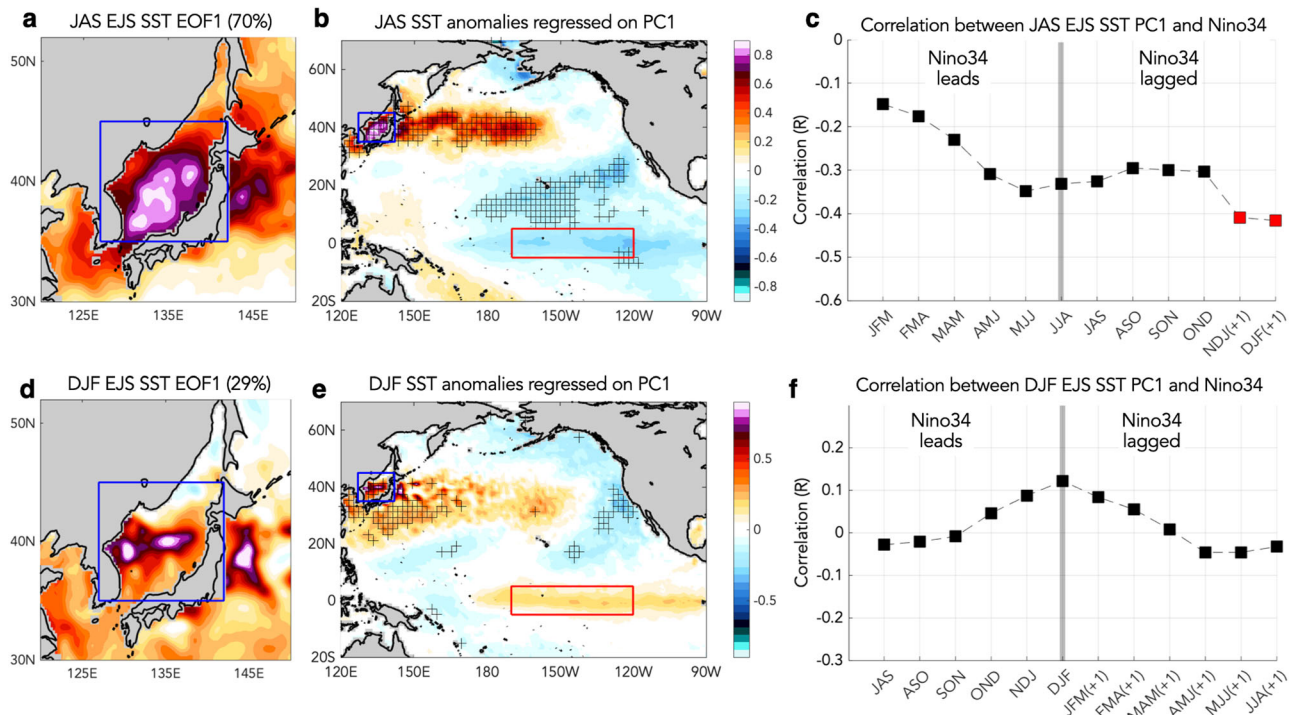


Fig. 2 | Seasonality of EJS SST variability and its relation with tropical Pacific SST. **a** Summer season (JAS) SST anomalies regressed on the leading principal component (PC1) of JAS EJS SST variability from EOF analysis. Blue box denotes the EJS region used in EOF analysis. **b** Zoomed-out version of **(a)**, showing the North and tropical Pacific SST anomalies associated with JAS EJS SST PC1. The Niño-3.4 region [5°S–5°N, 170°–120°E] is denoted as a red box. **c** Correlation coefficient between JAS EJS SST PC1 and seasonal Nino34 SST timeseries (area-averaged

SST anomalies over the Nino34 region). Red triangles indicate statistically significant skill at the 5% level based on a two-sided *t*-test using an adjusted degrees of freedom (see Methods). **d–f** Same as **(a–c)**, but for winter season (DJF) SST. In **(b)** and **(e)**, plus signs indicate regression coefficients that are statistically significant at the 5% level based on a two-sided *t*-test for which the temporal degrees of freedom are adjusted for autocorrelation (see Methods).

anomalies. The marginally significant correlations are only found when the EJS warm events lead the cold Nino3.4 SST anomalies (e.g., La Niña) by ~5–6 months (red rectangles in Fig. 2c). The correlation analyses imply that the EJS SST variability might not necessarily be driven by ENSO but could be associated with initial conditions of development of tropical SST anomalies.

Prediction skill for seasonal EJS SST anomalies

Using the SPEAR seasonal forecast system, we show the potential predictability and skillful prediction of seasonal EJS SST anomalies (Fig. 3). Seasonal EJS SST forecasts exhibit significant anomaly correlation coefficient (ACC) skill for lead times up to 9 months when they target forecast spring to late fall (Fig. 3a). With the exception of boreal winter (i.e., November–December–January to February–March–April), most seasonal forecasts yield significant prediction skills above persistence skill for 7 months or more (blue triangles in Fig. 3a). While both the internal and external forcing components (i.e., linear SST trend) contribute to seasonal prediction skill in the summer season EJS SST (Fig. 3b), without external forcing (black line), long lead (>8 months) forecasts initialized in winter (e.g., December–January–February, DJF) can provide added forecast skill (blue triangles in the black line in Fig. 3b). Specifically, the forecast skills drop quickly and show no significant skill above persistence for lead times up to 7 months, but the ACC skill is significantly higher when the forecasts are initialized in winter (8–9-month lead times). The 1-month lead (Fig. 3c) forecast confirms its successful detection of interannual variability of JAS EJS SST anomalies ($R = 0.95$, $p < 0.01$). The 8-month lead forecast (Fig. 3d) that is initialized in DJF-1 (i.e., the mean of forecasts initialized in December, January, and February) also shows a significant correlation ($R = 0.46$, $p < 0.05$), where the forecasted SST anomalies reveal low-frequency

fluctuations. Given the consistent skillful prediction of forecasts initialized in the winter seasons (blue triangles in the black line in Fig. 3b), we hypothesize that dynamical processes from the previous winter may serve as a source of predictability for the summer season EJS SST.

Prolonged air-sea coupled anomalies linked to summer EJS SST

To explore previous winter conditions that favor the development of summer EJS SST events, we examine seasonal evolutions of oceanic and atmospheric anomalies associated with the JAS EJS SST. In Fig. 4, we present seasonal correlation maps of JAS EJS SST time series with lags (1–6 months), where the reduced significance level (e.g., at the 10% level) is used to indicate potential sources of summer EJS SST predictability. As recent studies^{9,17} indicated, during summer, a strong atmospheric high-pressure system over the Northwestern Pacific (Fig. 4a) is accompanied by anomalous warm EJS SST (Fig. 4b). Figure 4a describes not only the increase in summer EJS solar radiation but also the possible engagement between the anticyclonic circulation and wave propagations over the Northwestern Pacific in prior seasons. The regional atmospheric anomalies appear to be an evident driver of summer EJS SST events, where the climatological winds are weak, and the mixed layer depth is relatively shallow. However, we note that the seasonal progression of those local atmospheric anomalies shows limited memories and short persistence confined to the summer. The lack of significant atmospheric anomalies over the EJS in prior seasons (i.e., April–May–June, AMJ in Fig. 4a) indicates that while the local atmospheric driver is the dominant contributor of anomalous EJS SST, it cannot be the source of long-lead predictability that yields significant prediction skills in the dynamical forecast system (Fig. 3b).

On the other hand, we focus on the development of summertime (July–August–September, JAS) EJS SST with a notable seasonal SST progression

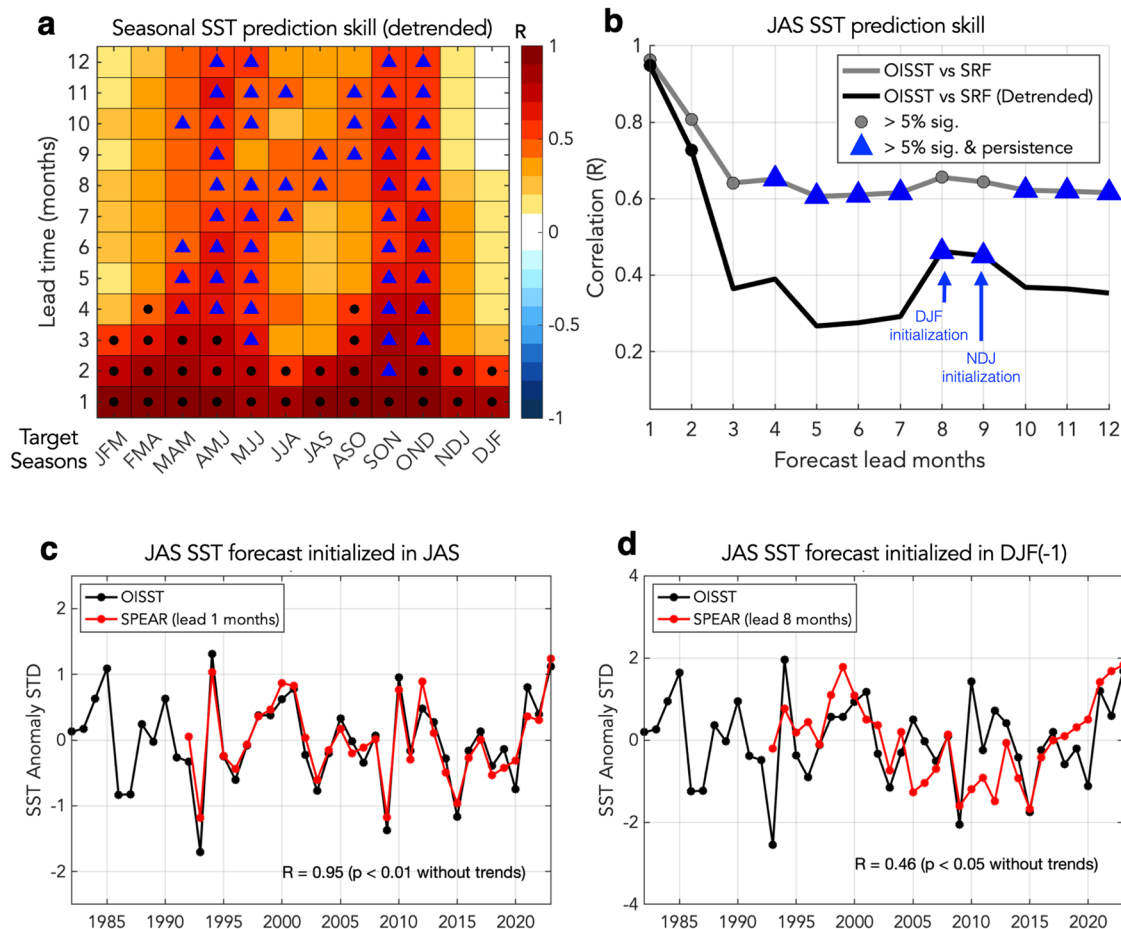


Fig. 3 | Skill of EJS SST predictions in GFDL SPEAR seasonal forecast system. **a** SST skill, where SST is linearly detrended, for the 15-member-ensemble SPEAR seasonal forecast, where seasons being predicted (target seasons) are on the x-axis, lead time months are on the y-axis, and anomaly correlation coefficients (ACC) of EJS SST are in color. Dots indicate statistically significant skill at the 5% level based on a two-sided t-test using adjusted degrees of freedom. Blue triangles denote significant skill above persistence (95% confidence level). **b** Anomaly Correlation

Coefficient (ACC) skill for the summer season (JAS) EJS SST forecasts with (gray line) and without (black line) the linear SST trend as a function of forecast lead months. Dots and blue triangles are the same as (a). Comparisons of the observed and forecasted time series of the summer season (JAS) EJS SST anomalies. Forecasts initialized in JAS at 1-month lead time (c) and DJF (-1) at 8-month lead time (d) are shown.

(Fig. 4b), where the warm SST anomalies gradually evolve from lower latitudes toward the north across the seasons. The significant seasonal SST migration suggests that the summer EJS SST might not purely result from the abrupt heat gained by local solar radiation but may be affected by lateral ocean heat advection. To confirm this, we continue to show seasonal progressions of surface wind and meridional Ekman transport anomalies. In Fig. 4c, d, the significant wind (Fig. 4c) and northward Ekman transport (Fig. 4d) anomalies are persistent over the East China Sea from winter (DJF-1) to the following summer (JJA). We suggest that northward advection driven by the anomalous easterlies over the East China Sea can be closely associated with the significant SST anomalies traveling from the lower latitude toward the EJS region. The persistence of the surface wind anomalies over the several months indicates that those local wind anomalies might not be a stochastic forcing but could be linked to large-scale climate variability. In the next section, we explore the connection between the summer EJS SST and large-scale climate variability on seasonal time scales.

Seasonal covariability between EJS SST and global surface wind anomalies

To identify climate components that maximize the covariance and related predictability between the EJS and global atmospheric fields, we conduct a singular value decomposition (SVD; see Methods for more details) analysis. Given the potential role of previous winter oceanic and atmospheric

conditions (Figs. 3d and 4), we use previous winter (NDJ-1) global surface wind speed anomalies and summer (JAS) EJS SST to compute the SVD (Fig. 5a)¹⁹. Using DJF-1 or NDJ-1 wind speed anomalies for the SVD analysis reveals no significant differences (not shown), so we use NDJ-1 winds to detect longer-lead predictability. To suppress ENSO impacts, although they might be negligible (Fig. 2), we compute SVD analysis after applying and removing linear regressions onto the concurrent and lagged (1–3 month) tropical Pacific SST variations, such as Nino3 [5°S–5°N, 150°–90°E] and Nino4 [5°S–5°N, 190°–150°E] SST time series, from the anomaly fields used in SVD analysis (Fig. 5).

We first show that the leading SST expansion coefficient (EJS SST SVD1) is found to be almost identical with the area-averaged EJS SST anomaly timeseries ($R = 0.99$; black and red lines in Fig. 5b), confirming that the first SVD mode successfully captures the most dominant summer EJS SST variability. Note that the two expansion coefficients for the leading SVD mode exhibit an exceptionally significant correlation ($R = 0.83$, $p < 0.001$; compare red and blue lines in Fig. 5b). The strong covariability appears to be attributed to both the interannual and multi-decadal time scales shown in the expansion coefficient timeseries. A squared covariance fraction (27%) explained by the first SVD mode indicates that a robust linear relationship exists between the summer EJS SST and the previous winter wind field.

Next, we consider the SVD1 global wind speed (NDJ-1) as a potential precursor of the summertime EJS SST and show associated SST and

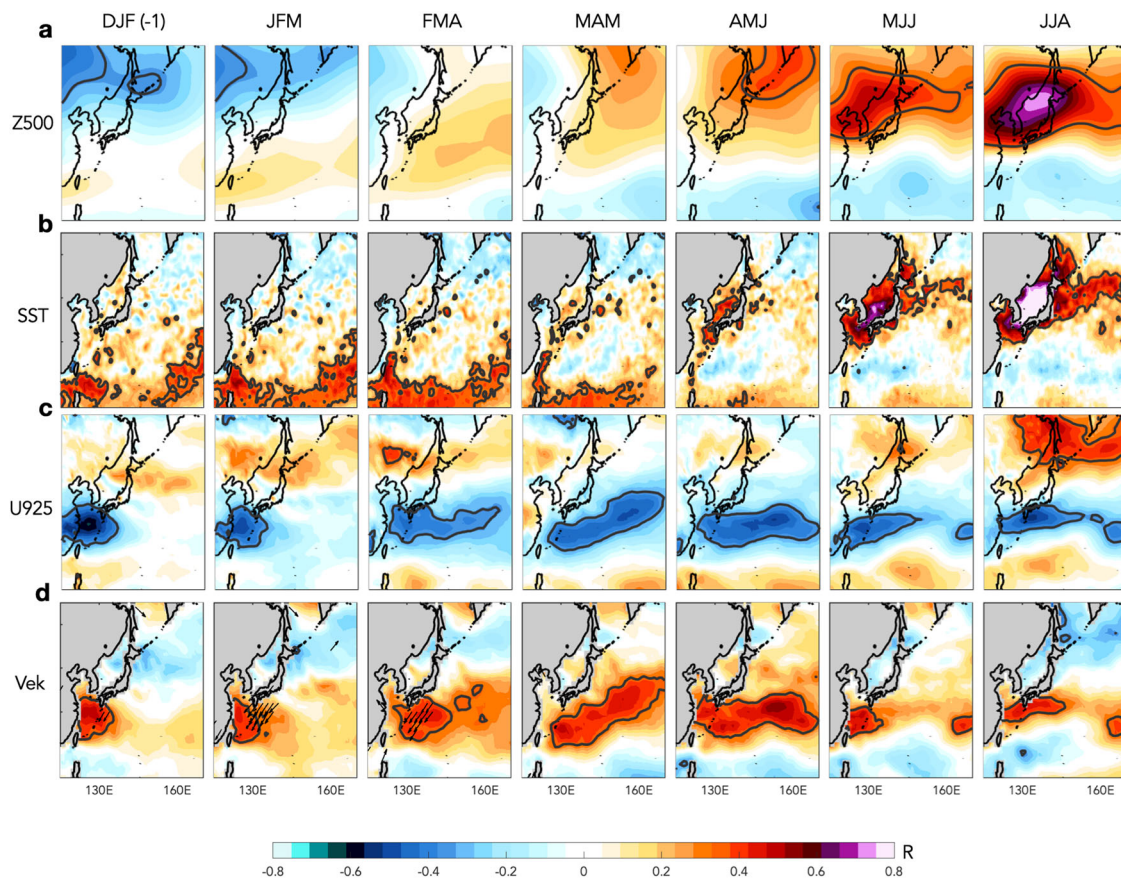


Fig. 4 | Spatial patterns of the summer season (JAS) EJS SST variability.

a–d Seasonal progression of oceanic and atmospheric anomalies associated with JAS EJS SST from the previous winter (DJF–1, left) to summer (JJA, right). Correlation maps between seasonal 500 hPa geopotential height (**a**), SST (**b**), 925 hPa zonal wind (**c**), and meridional Ekman transport (**d**) anomalies and the summer season (JAS)

EJS SST time series. Black contours denote where the correlation coefficients are statistically significant at the 10% level based on a two-sided *t*-test using an adjusted degrees of freedom.

atmospheric anomalies in Fig. 5c–j. The left and right columns exhibit the prior winter and following summer anomalies, respectively, that are regressed onto the SVD1 wind speed time series (blue line in Fig. 5b). The prior winter SST pattern (Fig. 5c) shows that the anomalous warm anomalies are characterized by the enhanced warming of the subtropical gyre over both the North Pacific and the North Atlantic. Winter wind patterns (Fig. 5d, e) show strong basin-scale easterlies over the subtropical and western Pacific and, most importantly, include the East China Sea wind anomalies (green box in Fig. 5d). The time evolutions of previous winter East China Sea wind anomalies exhibit a significant covariability with the summertime EJS SST anomalies ($R = 0.52$; black and green lines in Fig. 5b) as well as SVD1 wind speed time series ($R = 0.55$; blue and green lines in Fig. 5b), especially for the recent period. The previous winter East China Sea easterlies (green box in Fig. 5d) appear to be a part of the large-scale wind climate mode and serve as a physical agent conveying impacts of the wind-induced oceanic anomalies towards the EJS region. The mid-tropospheric atmosphere (Fig. 5f) indicates considerably significant high-pressure anomalies over the high-latitude, especially over the Barents Sea region, accompanied by signatures of the mid-latitude wave. Given the suggested connection between the prolonged East China Sea wind anomalies and the large-scale climate mode, we further examine the related impacts of anomalous circulations over the Barents Sea in the next section.

Investigation on winter large-scale atmospheric forcing of summer EJS SST

In this study, we propose the potential role of winter Barents Sea atmosphere variability (Fig. 6a) in contributing to the long-lived easterly and northward

Ekman Ocean heat transport anomalies over the East China Sea (Fig. 4b–d). In Fig. 6b, we describe similar temporal variations between the Barents Sea geopotential height (green) and SVD1 global wind speed anomalies (blue). During winter (e.g., NDJ and DJF in Fig. 6c and d), the strong anticyclonic and cyclonic circulation anomalies over the Barents Sea and Northeast Asia, respectively, are consistently shown, which appear to be linked to the mid-latitude atmospheric anomalies between 20° – 40° N. From late winter to spring (e.g., JFM + 1 to MAM + 1 in Fig. 6c, d), those zonally extended high-pressure anomalies are enhanced and shifted toward the pole, especially over the North Pacific Ocean. After spring (e.g., MJJ + 1 to JJA + 1 in Fig. 6c, d), the mid-latitude high-pressure anomalies are found to persist. The notable difference is that the SVD1 global wind speed (e.g., JJA + 1 in Fig. 6c) captures the much stronger magnitude of anticyclonic circulations over the EJS compared to that of Barents Sea atmospheric variability (e.g., JJA + 1 in Fig. 6d). We attribute this difference to the maximized covariance captured in SVD analysis that extracts both signals of the summer EJS SST variability and its related atmospheric forcing.

The mid-latitude atmospheric anomalies shown in Fig. 6 appear to be associated with large-scale air-sea interactions over the Northwestern Pacific. Both correlation maps of 10 m wind speed SVD1 (Fig. 7a) and Barents Sea High (Fig. 7c) exhibit the prolonged surface wind speed anomalies over the East China Sea from NDJ to MAM + 1. In response to surface wind anomalies, the poleward Ekman transport is found, where the location of ocean gyre warming is moved across the seasons over the North Pacific (Fig. 7b and d). Note that the northward migration of warm SST along the western boundary (e.g., Kuroshio) from winter to the following summer

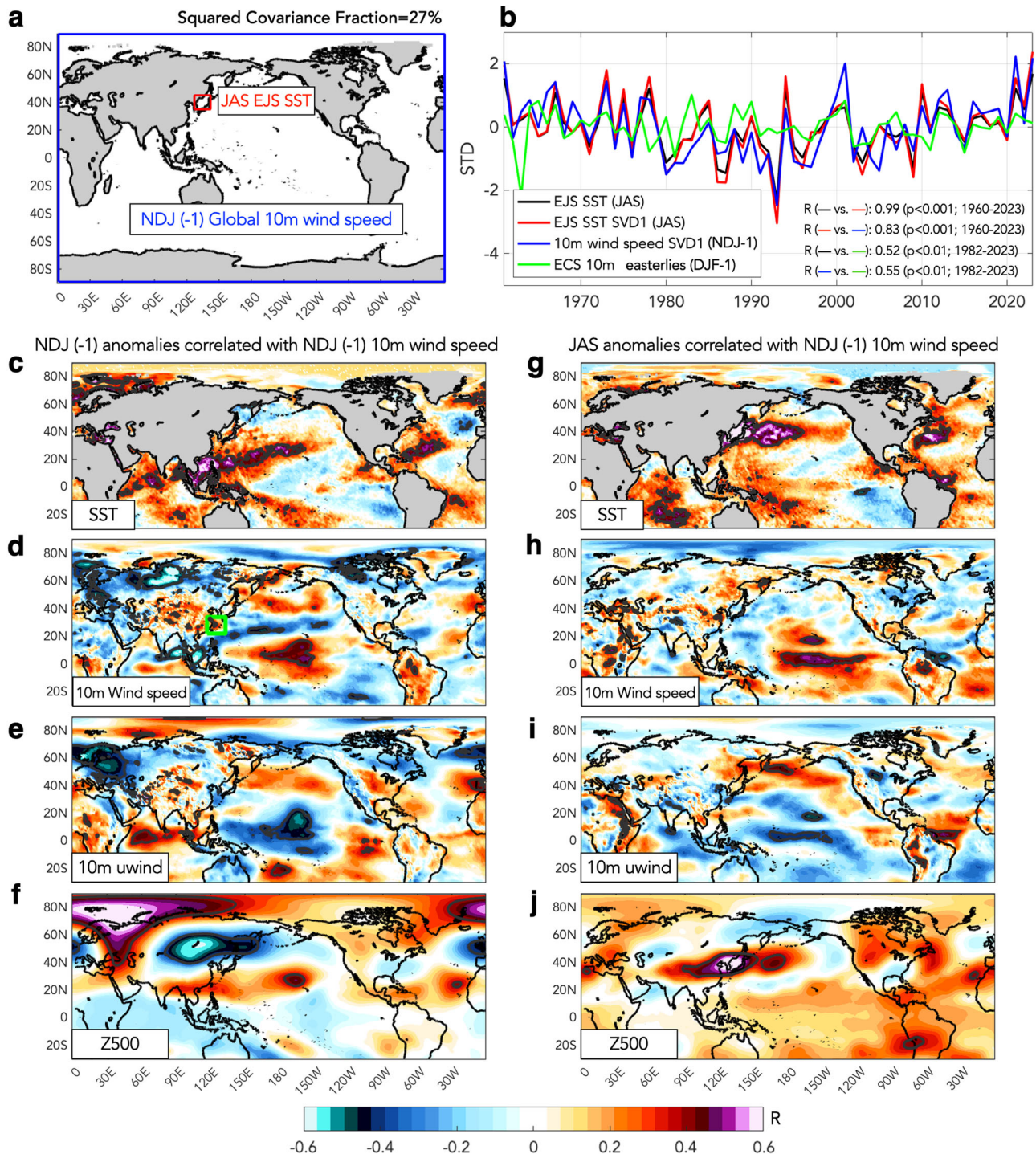


Fig. 5 | Singular vector decomposition (SVD) analysis to identify linkages between the summertime EJS SST and large-scale atmospheric anomalies during the prior winter. **a** The map to show the regions used in SVD analysis. SVD analysis is conducted where linear regressions onto the ENSO signals (i.e., Niño3 SST [5°S–5°N, 150°–90°E] & Niño4 SST [5°S–5°N, 190°–150°E]) are applied and removed from all anomaly fields. Summer (JAS) season SST anomalies over the EJS (red box) and prior winter (NDJ-1) global 10 m wind speed anomalies (blue boxes) are used for SVD computation. The squared covariance fraction of the leading SVD mode is given at the top of the panel. **b** Time series associated with summertime EJS SST variability. Normalized time series of JAS EJS SST anomalies (black), SVD expansion

coefficients for SST (red) and wind speed (blue) of the leading SVD mode, and DJF (-1) ECS 10 m zonal easterly anomalies (green) are shown. Values shown in the bottom right indicate the correlation coefficient between a pair of time series. **c–f** Correlation maps between the expansion coefficient time series of NDJ (-1) global wind speed (blue line in **b**) and prior winter (NDJ-1) SST (**c**), 10 m wind speed (**d**), 10 m zonal wind (**e**), and 500 hPa geopotential height (**f**) anomaly fields. **g–j** Same as **c–f** but for summer (JAS) anomaly fields. In **c–h**, Black contours denote where the correlation coefficients are statistically significant at the 5% level based on a two-sided t -test using an adjusted degrees of freedom.

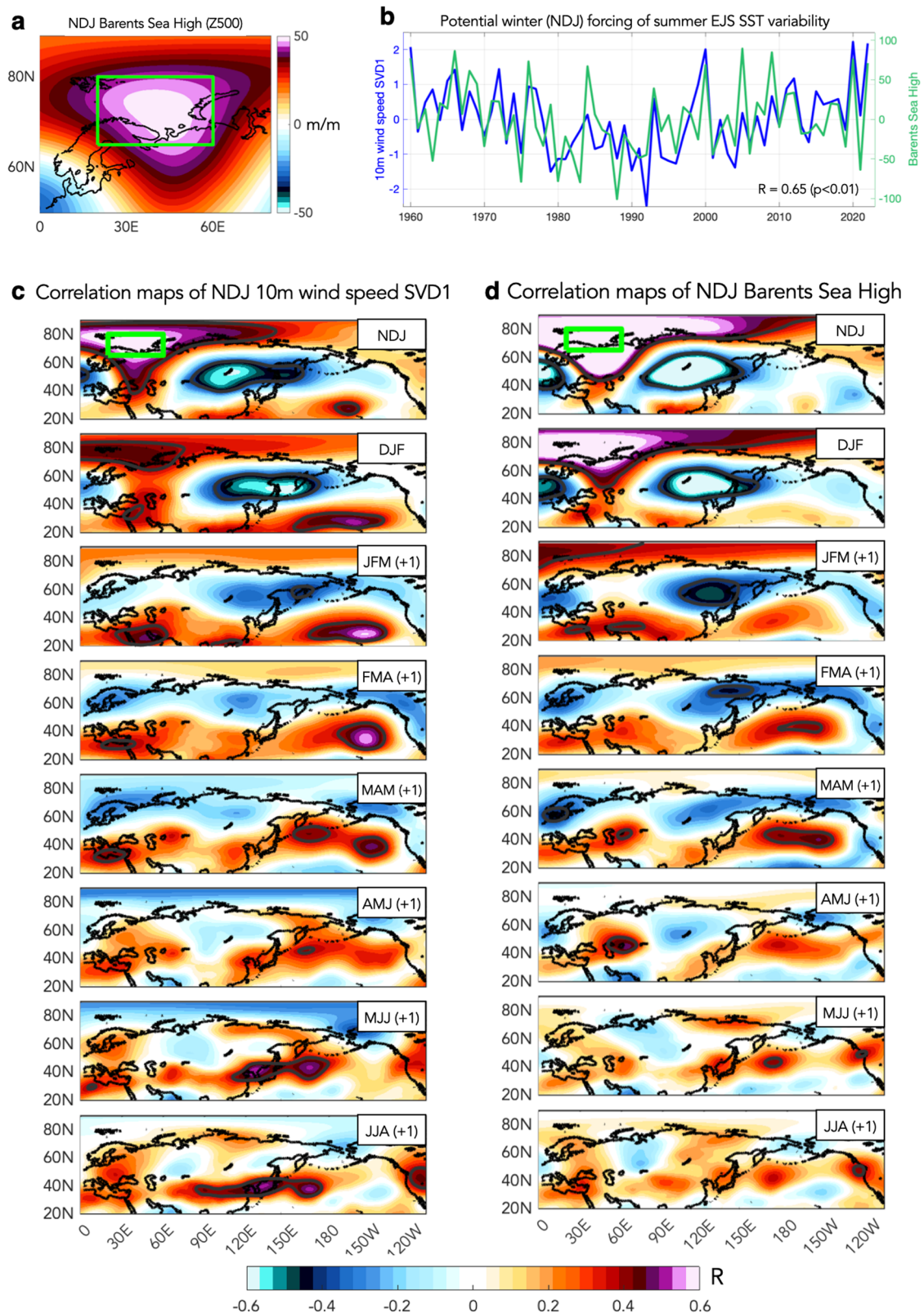


Fig. 6 | Potential source of long-lead predictability of summer EJS SST variability. **a** Winter (NDJ) Barents Sea High pattern computed as regression coefficients of NDJ 500 hPa geopotential height (Z500) anomaly field with the NDJ Barents Sea Z500 time series, where the time series is computed as area-averaged Z500 anomalies of NDJ Barents Sea ([20°–60°E, 65°–80°N], green box). **b** Comparison of time series between NDJ 10 m wind speed SVD1 (blue line) and Barents Sea High (green) for the

period between 1960 and 2022. **c** Seasonal progressions of 500 hPa geopotential height anomalies correlated to the expansion coefficient time series for NDJ global wind speed leading SVD mode (**c**) and NDJ Barents Sea Z500 time series (**d**). In (**c**, **d**), black contours denote where the correlation coefficients are statistically significant at the 5% level based on a two-sided *t*-test using an adjusted degrees of freedom.

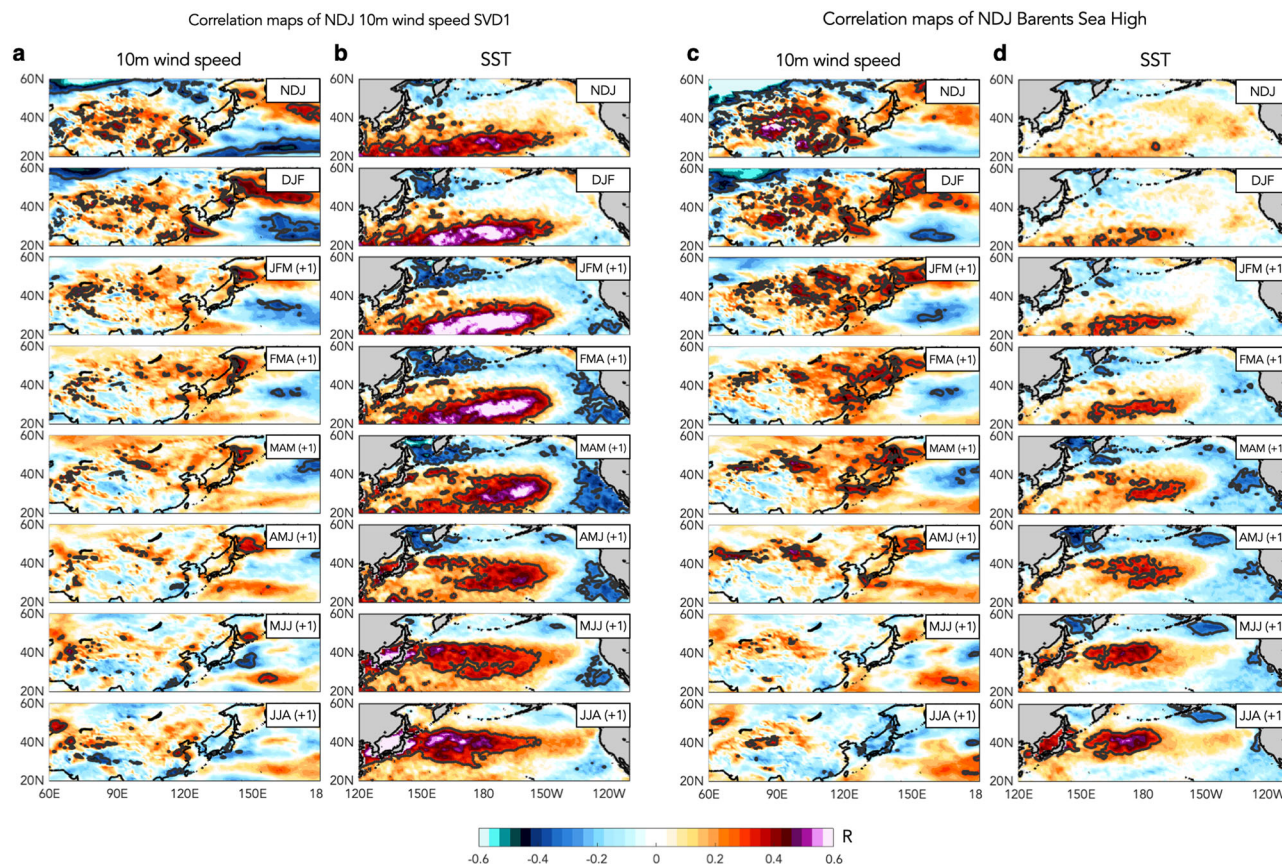


Fig. 7 | Persistence of surface wind anomalies over the East China Sea and associated oceanic response. a, b Seasonal progressions of 10 m wind speed (a) and SST anomalies correlated to the expansion coefficient time series of NDJ global wind speed leading SVD mode. **c, d** Same as (a, b) but for the NDJ Barents Sea Z500 time

series (green line in Fig. 6b). In a–d, black contours denote where the correlation coefficients are statistically significant at the 5% level based on a two-sided *t*-test using an adjusted degrees of freedom.

(Fig. 7b and d) is highly consistent with the SST progression of summer EJS SST described in Fig. 4b.

To support the proposed physical linkage between the summer EJS SST progression and regional/global wind forcing, Fig. 8 shows the similar SST progressions reconstructed by the winter East China Sea surface easterlies (green line in Fig. 5b) and the SVD1 global wind speed expansion coefficient (blue line in Fig. 5b). All the seasonal SST progressions (Figs. 4b and 8a, b) indicate that the subtropical warm anomalies move toward the mid-latitude along the western boundary, entering and affecting the EJS during spring seasons. A similar northward migration of warm water is also confirmed in the SPEAR seasonal forecast system (Fig. 8c). Compared to other progression maps (Fig. 8a, b), Fig. 8c reveals the less deterministic and slower ocean advection, especially over the Korea strait (yellow box) during spring (MJJ + 1) to summer (JAS + 1), implying that a relatively coarse ocean resolution (e.g., 100 km) of the dynamical forecasts might not be enough to resolve the realistic ocean propagation. However, the initial significant warm anomalies sitting over the East China Sea during DJF-1 and the northward propagation along the western boundary across the seasons support our hypothesis that the oceanic driver may play a role in providing the long-lead predictability of summertime EJS SST. In Fig. 8d, the positive sea surface height (SSH) anomalies, indicative of increased ocean heat content, also reveal that the northward oceanic horizontal heat advection could contribute to an increased mean SST state that can enhance and favor the summertime EJS SST warm events. Both observations and the seasonal forecast system support our hypothesis that the wind-induced Ekman transport over the East China Sea can yield long-lead predictability of summer EJS SST events.

Seasonal evolutions of EJS Marine heatwave events in summer 2021

While the atmospheric forcing, such as an atmospheric ridge (e.g., anticyclonic circulations)^{7,10}, has been described as the dominant driver causing the significant amplitude of summer EJS warm SST anomalies (also MHWs)¹⁷, our findings reveal that the air-sea couplings in prior seasons can be also important in understanding and predicting the summer EJS SST events. For example, the long-lived ocean temperature anomalies during spring and previous winter can contribute to summer EJS SST events by affecting the SST mean state. To hint at seasonal physical drivers of EJS SST anomalies, we present a heat budget analysis of the upper-ocean of 2021 EJS SST in Fig. 9, which was one of the record-breaking MHW events in the historical record¹⁷. The budget equation is derived from the mixed-layer temperature (MLT) equation (see Methods for more details) with a time-varying mixed-layer depth (MLD). In Fig. 9a, the 2021 July EJS MHW event is developed through prolonged and persistent warm anomalies since April (positive MLT tendency, $dT/dt > 0$; black line), where the area-averaged daily temperature (dT/dt) increases are frequently higher than mean climatological variations (gray shading). As described in previous findings^{4,7,10,17}, the downward heat flux (Q ; orange line in Fig. 9a) is the most dominant term in driving MLT tendency during summer (e.g., June and July). Supportingly, Fig. 9b reveals that the spatial structures of summer (e.g., June, July) MLT tendency are significantly explained by heat flux terms. The EJS MLT tendency during spring (e.g., March to May), however, can be largely contributed by ocean mixing (MIX) or advection (HADV). We especially note that March MLT tendency seems to be determined by the horizontal advection term (HADV). The significantly prolonged EJS SST

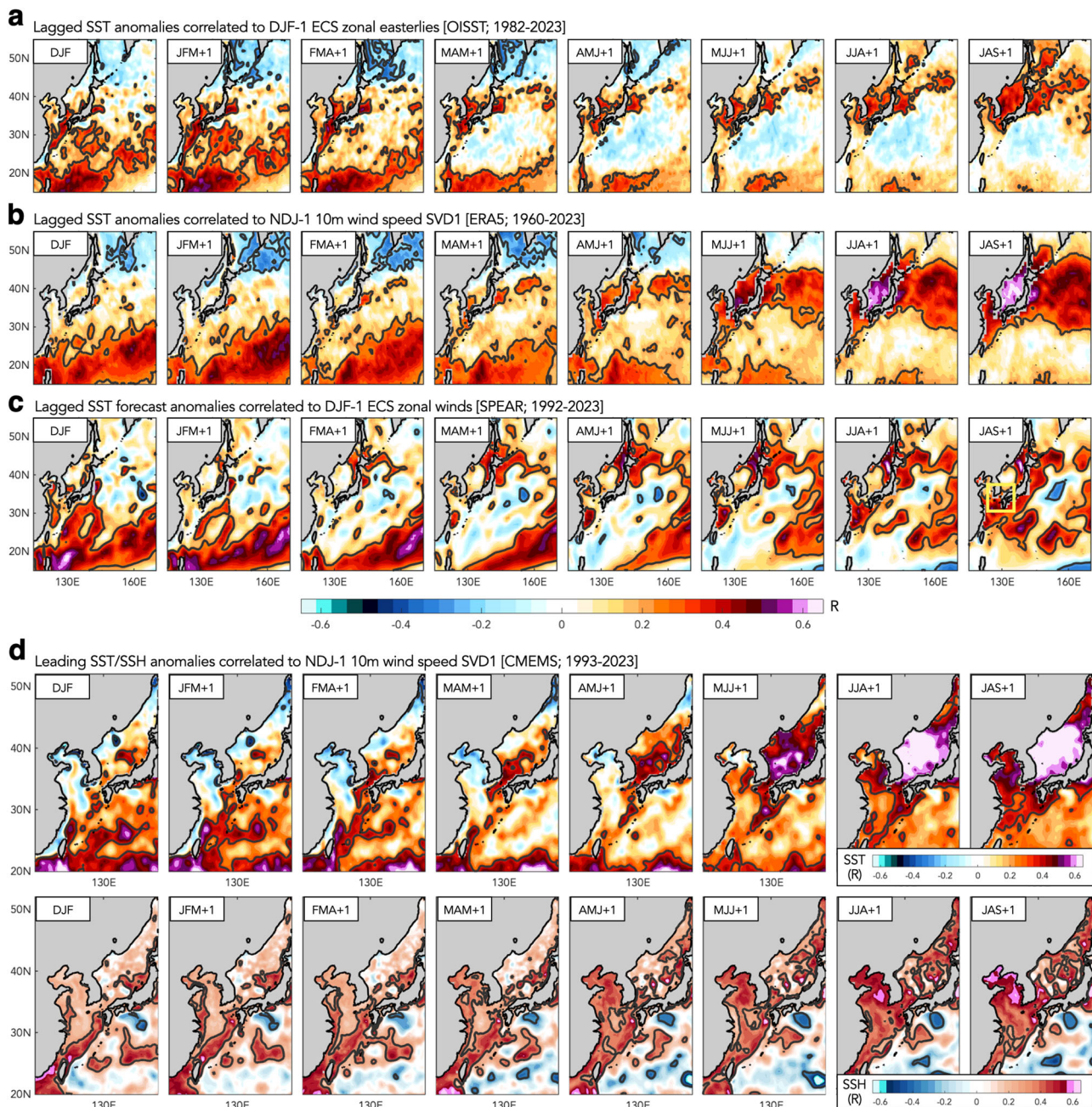


Fig. 8 | Predictability of summer season (JAS) EJS SST variability. **a** Maps of correlation coefficients between lagged seasonal SST anomalies and the DJF-1 East China Sea easterly anomaly timeseries (green line in Fig. 5b). **b** Same as **a** but with the expansion coefficient time series for NDJ (-1) global wind speed leading SVD mode (blue line in Fig. 5b). **c** Same as **a** but of SST forecasts initialized by DJF. The yellow box in the rightmost panel denotes the Korea strait, which is a sea passage between

Korean and Japan. **d** Maps of correlation coefficients between the SST (top) SSH (bottom) anomalies and the NDJ (-1) global wind speed leading SVD mode (blue line in Fig. 5b). Black contours denote where the correlation coefficients are statistically significant at the 10% level based on the adjusted degrees of freedom and a two-tailed Student's *t*-test.

warm anomalies since April (Fig. 9a) indicate that summer MHW events can be affected by prior seasons' ocean mean state, through oceanic advection anomalies.

Predictability of summer EJS SST

Finally, we show that both the atmospheric and oceanic drivers can significantly affect and help predict the summertime EJS SST (Fig. 10). The June-July-August (JJA) shortwave solar radiation (Fig. 10a) over the EJS region (Fig. 10b) shows a significant correlation with the JAS EJS SST ($R = 0.65$, $p < 0.01$); however, it is notable that the recent heat flux variability cannot explain the latest record-highs of the EJS

SST (i.e., 2021-2023 in Fig. 10a). For the recent decades, we find that the northward surface seawater velocity (Fig. 10c) over the Korean Strait (black box in Fig. 10d) can significantly contribute to the JAS EJS SST ($R = 0.53$, $p < 0.05$) at three months prior to the summer EJS SST events. The significant contribution of the northward sea water velocity to the summer EJS SST is in great agreement with the results from the present study. Given that the independent relationship between solar radiation and ocean velocity temporal evolutions is found ($R = 0.07$), we highlight the benefit of using both atmospheric and oceanic drivers to predict the summertime EJS SST. Using a multiple linear regression model, we reconstruct the summer season

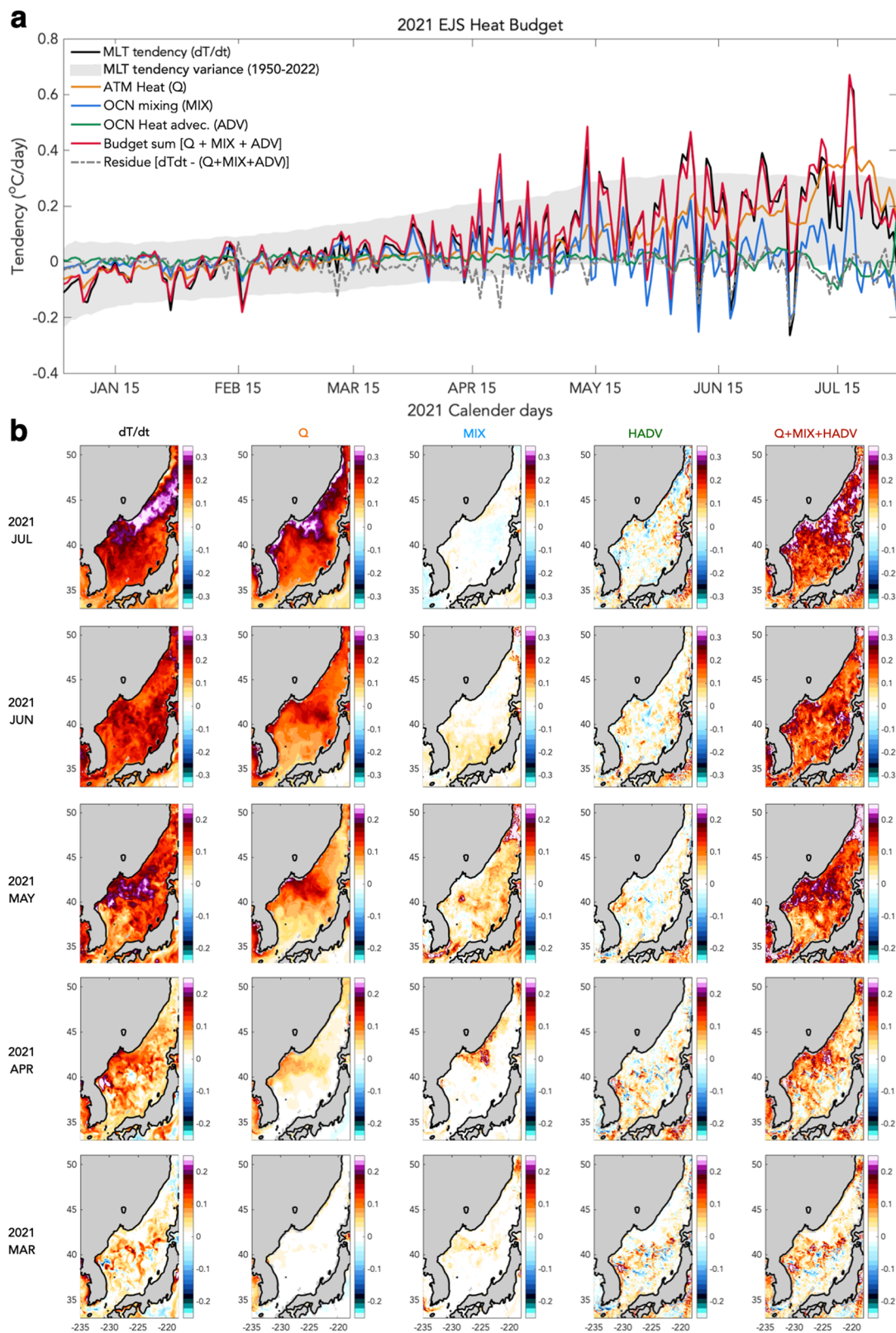


Fig. 9 | Mixed layer budget estimated for 2021 EJS in observations. a Budget terms ($^{\circ}\text{C}/\text{day}$) of EJS, including mixed layer temperature tendency (dT/dt , black), long-term dT/dt variability represented as 1.5 standard deviations for the period 1950–2022 (shading), total surface heat flux (Q , red), ocean mixing (MIX , blue) and advection, (ADV , green), the sum of budget terms ($Q + MIX + ADV$, red), and the residual (Residue, dashed gray). All time series are area-weighted averaged using daily ocean temperature for the EJS. **b** Spatial maps of monthly averages of each budget term, which are shown in for July, June, May, April, and March.

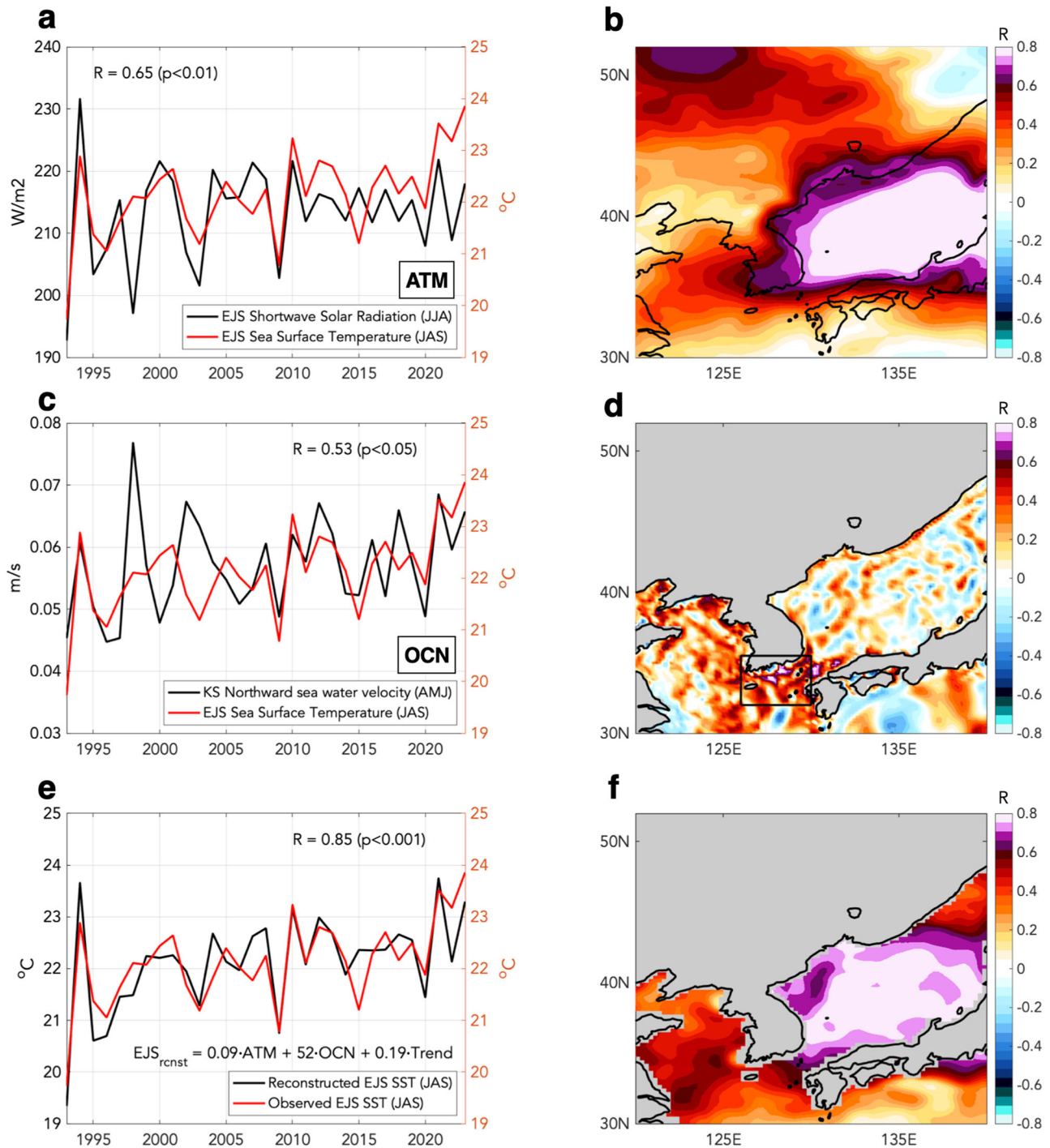


Fig. 10 | Contributions of atmospheric and oceanic anomalies on the EJS SST variability. **a** Timeseries of area-averaged June-July-August (JJA) shortwave solar radiation flux (W/m^2 ; black) and July-August-September (JAS) SST ($^{\circ}\text{C}$; red) over the EJS. **b** The correlation map of JJA shortwave solar radiation flux field and the timeseries of the black line in **a**. **c**, **d** Same as (**a**, **b**) but for area-averaged April-May-June northward surface sea water velocity field (m/s). The black box in (**d**) denotes the Korea strait region [32° - 35.5°N & 126° - 130°E]. **e** Observed ($^{\circ}\text{C}$; red) and

reconstructed ($^{\circ}\text{C}$; black) summer season EJS SST timeseries based on multiple linear regression with suggested predictors. In reconstruction, black lines in (**a**) and (**c**) and JAS EJS SST trend ($1.06^{\circ}\text{C/decade}$) are used. The computed corresponding linear regression values are 0.09, 52, and 0.19 for the atmospheric, oceanic, and warming component, respectively. **f** The correlation map of JAS SST field and the timeseries of the black line in (**e**).

EJS SST timeseries based on those physical drivers and the summer season EJS SST trend ($1.06^{\circ}\text{C/decade}$) and compare it with the observed timeseries in Fig. 10e. The JJA EJS solar radiation, AMJ northward sea water velocity, and JAS EJS SST trend are used with the computed regression coefficients shown in Fig. 10e. We find that the reconstructed index explains the considerable variance of the

summer season EJS SST variability ($R = 0.85$, $p < 0.001$), and the related SST anomaly pattern (Fig. 10f) has a great similarity to the summer EJS SST pattern shown in Fig. 2a. Without the linear SST trend component, the predictor based on the JJA EJS solar radiation and AMJ northward sea water velocity shows the improved correlation skill ($R = 0.75$, $p < 0.001$; not shown), indicating that the

oceanic anomalies can provide added forecast skill for the summertime EJS SST along with the atmospheric component.

Discussion

The present study investigates prediction skills and the related source of predictability for the summer season EJS SST variability. A close examination of the development of summertime EJS SST anomalies, using correlation maps, SVD analysis, and budget analysis, indicates that a significant linear covariance exists between the summer (JAS) EJS SST and global atmospheric anomalies during the previous winter (e.g., NDJ-1 or DJF-1). Specifically, winter large-scale atmospheric circulations linked to Barents Sea atmospheric variability are found to induce persistent surface wind and associated northward Ekman heat transport anomalies over the East China Sea. The anomalous ocean advection develops and enters the EJS region across the seasons, contributing to the summer SST anomalies. Our study proposes that the slow-evolving oceanic anomalies associated with the local and large-scale air-sea coupling during the previous winter can serve as a source of the summer EJS SST predictability by modulating the basin's SST mean state. Supporting the observational results, the GFDL SPEAR seasonal forecast system demonstrates the skillful forecast of summer EJS SST when initialized in winter, revealing that the current forecast system can skillfully predict the summertime EJS SST events 8–9 months in advance.

The role of the global winter atmospheric circulation associated with the Barents Sea variability in this study supports previous findings^{20,21}. The atmospheric feedback to Barents-Kara sea-ice loss during winter has been known to significantly affect Northern Europe and eastern Asia during cold seasons. Supporting the recent findings from Xu et al.²¹, our results indicate that the Barents Sea high-pressure anomalies, which might be associated with Barents Sea's sea-ice reduction, appear to excite long Rossby wave trains that propagate downstream to the Eurasia continent and North Pacific (Fig. 6). Although the present study leaves the question of how the wave train activity persists over the months, driving significant changes in the Northwestern Pacific oceanic and atmospheric anomalies, our findings present a clear engagement and participation of large-scale decadal climate modes in seasonal EJS SST fluctuations. The distinct low-frequency component shown in the summer EJS SST, 10 m wind speed SVD, and the Barents Sea high temporal variations (Figs. 5b and 6b) is also similar to that of North Atlantic variability, especially the Atlantic Multidecadal Oscillation²². Previous findings^{22,23} have shown that the North Atlantic warming can also modulate the North Pacific SST anomalies through atmospheric teleconnections (e.g., upper-level divergence in the North Atlantic and compensating subsidence in the North Pacific). The detailed examination of the seasonal evolution of the winter large-scale climate variability associated with the Barents Sea variability should further be investigated; thus, the present study can be followed by many remaining questions, such as: Has the large-scale wind forcing of EJS SST been stationary over time? What would be their projected changes in intensity or spatial structure in a warming climate? Could the same global wind anomalies be used as a potential source of predictability for other regions or climate modes (e.g., Other East Asian marginal seas or Kuroshio–Oyashio Extension), too?

Suggesting that increasing ocean resolution might improve the EJS SST prediction by better resolving the regional ocean advection (e.g., Korea Strait), we also highlight that the implication of detection of those mechanisms in the low-resolution model provides many potential applications using our understanding of basin-to-hemispheric scale ocean/atmospheric circulations. Our study illustrates that once the ocean is actively involved in the mechanisms, it can yield long-lead predictability through longer persistence and slow evolutions associated with air-sea coupled processes. The significant long-lead forecasts initialized in winter for predictions of summer EJS SST shed light on the implications and applications of the proposed mechanisms in improving the prediction of seasonal hydroclimate extreme events over the Northwestern Pacific.

Methods

Observational datasets

Observational datasets used in this study include monthly averages of NOAA's Optimum Interpolation Sea Surface Temperature (OISSTv2.1)²⁴ and European Center for Medium-Range Weather Forecasts Reanalysis-5 (ERA5)²⁵. OISST is used to validate SST seasonal forecasts and ERA5 product to examine variability and predictability SST and MHW events over the EJS using monthly averages of SST, 10 m zonal and meridional winds, 10 m wind speed, 500-hPa geopotential height. Both OISST and ERA datasets are available on 0.25° grids.

SPEAR Seasonal retrospective forecasts

As GFDL's real-time seasonal prediction system, SPEAR has contributed to the North American Multi-Model Ensemble (NMME) project²⁶ since 2021 (<https://www.cpc.ncep.noaa.gov/products/NMME/>). SPEAR Seasonal retrospective forecasts use the SPEAR_MED model²⁷, where the atmosphere/land resolutions are 50 km and ocean/ice resolutions are 1 degree with refinement to 1/3 degree in the tropics. A 15-member ensemble of SPEAR seasonal forecasts is available from 1992 to 2019 and 30-member from 2020 onward. Each forecast is initialized with a 30-member SPEAR's ocean data assimilation (ODA) for the ocean initial conditions and a 5-member SPEAR_MED coupled nudged simulations (SPEAR_MED_Nudged) for the atmospheric, land, and sea ice initial conditions. The ocean reanalysis ODA includes daily SST from OISSTv2, XBT data from the Global Temperature and Salinity Profile Program (GTSP)²⁸, and Argo temperature and salinity data²⁹ and applies a bias correction scheme (OTA) to reduce model drift²⁷. In the SPEAR_MED_Nudged run, atmospheric temperature, winds, and moisture were nudged toward the 6-hourly data from the Climate Forecast System Reanalysis (CFSR)³⁰ and sea surface temperature (SST) was restored toward the daily OISST²⁴. More details of SPEAR's ODA and seasonal retrospective forecasts can be found in Lu et al.²⁷. SPEAR seasonal prediction system has explored and shown significant forecast skill in predicting many key climate variability and extreme events, such as the Nino3.4 index²⁷, atmospheric rivers over Western North America³¹, Antarctic/Arctic sea ice^{32,33}, midlatitude baroclinic wave³⁴, Kuroshio Extension variability³⁵, North American winter temperature swing index³⁶, and North American summer and winter time temperature extremes^{37,38}.

Singular Vector Decomposition (SVD) analysis

To examine the source of predictability of the East/Japan Sea (EJS; 35°–45°N, 127°–142°E) SST events and their linkages to large-scale atmospheric fields, we conduct a singular value decomposition (SVD) analysis. The SVD analysis has been widely used to extract dominant modes of variability that fluctuate coherently in two variables^{19,39}. The SVD is similar to the ordinary EOF, except that a cross-covariance between two fields is used. In this study, we use summer (July–August–September, JAS) EJS SST and global wind speed anomalies during the prior winter (November–December–January, NDJ-1), focusing on their leading mode of SVD. Considering 8-month-lag covariance between SST and wind speed fields (e.g., SST is followed by wind speed), we assume the leading SVD mode of NDJ-1 global wind speed anomalies as the atmospheric forcing associated with EJS SST and MHW events during the following summer. The sets of normalized expansion coefficients (i.e., time series) for each SST and wind speed fields are used to explore physical mechanisms and evolutions of EJS SST and MHW events. The SVD analysis is computed after we apply and remove linear regressions onto the concurrent and lagged (1–3 month) tropical Pacific SST variations, such as Nino3 [5°S–5°N, 150°–90°E] and Nino4 [5°S–5°N, 190°–150°E] SST time series, from the anomaly fields.

Adjusted degrees of freedom

The significance test for correlations of timeseries (e.g., SVD expansion coefficients, anomaly correlation coefficients) in this study is based on adjusted degrees of freedom, which is associated with persistence (e.g., autocorrelation) or low-frequency signals (e.g., decadal variability). Following Bretherton et al.⁴⁰, we adopt adjusted degrees of freedom,

$$N^* = \frac{N}{1 + 2 \sum_{j=1}^{N-1} \left(1 - \frac{j}{N}\right) \rho_{xx}(j) \rho_{yy}(j)}$$

where N is the number of time steps, and $\rho_{xx}(j)$ and $\rho_{yy}(j)$ are the autocorrelation coefficient of time series x and y at lag j .

Heat budget analysis

The present study uses a heat budget analysis to identify and quantify local physical processes that contribute to changes in EJS SST. Following related literature^{41–43}, we calculate the rate of change in EJS SST, using mixed-layer temperature (MLT) tendency equation, referred to as the terms of the heat budget equation as follows.

$$\underbrace{\underbrace{\frac{\partial T_m}{\partial t}}_{\text{ML tendency}} + \underbrace{\underbrace{\frac{Q_{net} - Q_z}{\rho C_p h}}_Q - \underbrace{\mathbf{u}_m \cdot \nabla T_m}_{HADV}}_{\text{Entrainment/Detrainment}}}_{\text{MIX}} + \underbrace{\underbrace{-\frac{(T_m - T_{-h})}{h} \left(\frac{\partial h}{\partial t} + \mathbf{u}_{-h} \cdot \nabla T_m + w_{-h} \right)}_{\text{lateral induction}} + \underbrace{\nabla_h \cdot (K_h \nabla T_m) - K_v \frac{\partial T}{\partial z} \frac{1}{h}}_{\text{Horizontal \& Vertical mixing}}}_{\text{+Residual}} \quad (1)$$

Here, the mixed layer temperature tendency is expressed as the sum of the effects of the downward net heat flux (Q), horizontal advection ($HADV$), ocean mixing (MIX) that includes entrainment/detrainment and turbulent mixing, and the residual. In Eq. (1), T_m and \mathbf{u}_m are ocean potential temperature and velocities (u, v) averaged from the time varying mixed layer depth (MLD; h) to the surface. The heat flux term (Q) is calculated with the difference between Q_{net} , which is the sum of the shortwave and longwave radiation and latent and sensible heat fluxes, and the penetrating shortwave radiation Q_z . In Q , the reference density of seawater ρ and the specific heat of seawater at a constant pressure C_p are assumed as $\rho = 1025 \text{ kg m}^{-3}$ and $C_p = 3850 \text{ J kg}^{-1} \text{ K}^{-1}$, respectively. For the ocean advection term (ADV), only the horizontal advection ($HADV$) is considered. The entrainment velocity is expressed as the sum of temporal changes in MLD, lateral induction, and vertical advection⁴⁴. T_{-h} , \mathbf{u}_{-h} , and w_{-h} are the potential temperature and the horizontal and vertical velocity at the mixed layer depth h . In the horizontal and vertical turbulent mixing term, horizontal (K_h) and vertical (K_v) eddy diffusivity coefficients are assumed as the global averaged values, where K_h is $10^4 \text{ m}^2 \text{ s}^{-1}$ and K_v is $10^{-4} \text{ m}^2 \text{ s}^{-1}$ ⁴⁵.

Data availability

NOAA high resolution OISST v2.1 data were downloaded from the website of NOAA/OAR/ESRL PSL (<https://psl.noaa.gov/data/gridded/data.noaa.oisst.v2.html>). The ERA5 datasets were obtained from (<https://cds.climate.copernicus.eu/#/search?text=ERA5&type=dataset>). The SPEAR seasonal hindcast SST data are available at the NMME website (<https://www.cpc.ncep.noaa.gov/products/NMME>).

Code availability

All analysis were conducted using MATLAB. Codes generated by the present study are available from the corresponding author upon request.

Received: 16 May 2024; Accepted: 26 August 2024;
Published online: 08 September 2024

References

- Information, N. C. f. E. Annual 2023 Global Climate Report. <https://www.ncei.noaa.gov/access/monitoring/monthly-report/global/202313>, <https://www.ncei.noaa.gov/access/monitoring/monthly-report/global/202313> (2024).
- Information, N. N. C. f. E. Monthly Global Climate Report for August 2023. <https://www.ncei.noaa.gov/access/monitoring/monthly-report/global/202308> (2023).
- Wu, L. et al. Enhanced warming over the global subtropical western boundary currents. *Nat. Clim. Change* **2**, 161–166 (2012).
- Lee, S. et al. Rapidly changing East Asian marine heatwaves under a warming climate. *J. Geophys. Res.: Oceans* **128**, e2023JC019761 (2023).
- Hayashi, M., Shiogama, H. & Ogura, T. The contribution of climate change to increasing extreme ocean warming around Japan. *Geophys. Res. Lett.* **49**, e2022GL100785 (2022).
- Johnson, G. C. A. R. L. L. Global Oceans [in “State of the Climate in 2021”. *Bull. Amer. Meteor. Soc.* **103**, S143–S191 (2022).].
- Oh, H. et al. Classification and causes of east asian marine heatwaves during boreal summer. *J. Clim.* **36**, 1435–1449 (2023).
- Cai, R., Tan, H. & Kontoyannis, H. Robust surface warming in offshore China seas and its relationship to the East Asian monsoon wind field and ocean forcing on interdecadal time scales. *J. Clim.* **30**, 8987–9005 (2017).
- Choi, W. et al. Characteristics and mechanisms of marine heatwaves in the east asian marginal seas: regional and seasonal differences. *Remote Sens.* **14**, 3522 (2022).
- Wang, D. et al. Characteristics of Marine heatwaves in the Japan/East Sea. *Remote Sens.* **14**, 936 (2022).
- Dasgupta, P., Nam, S., Saranya, J. S. & Roxy, M. K. Marine heatwaves in the east asian marginal seas facilitated by boreal summer intraseasonal oscillations. *J. Geophys. Res. Oceans* **129**, e2023JC020602 (2024).
- Lee, E.-Y. & Park, K.-A. Change in the recent warming trend of sea surface temperature in the East Sea (Sea of Japan) over decades (1982–2018). *Remote Sens.* **11**, 2613 (2019).
- Hobday, A. J. et al. A hierarchical approach to defining marine heatwaves. *Prog. Oceanogr.* **141**, 227–238 (2016).
- Jacox, M. G. et al. Global seasonal forecasts of marine heatwaves. *Nature* **604**, 486–490 (2022).
- Song, S.-Y. et al. Wintertime sea surface temperature variability modulated by Arctic Oscillation in the northwestern part of the East/Japan Sea and its relationship with marine heatwaves. *Front. Marine Sci.* **10**, <https://doi.org/10.3389/fmars.2023.1198418> (2023).
- Lee, S., Park, M.-S., Kwon, M., Kim, Y. H. & Park, Y.-G. Two major modes of East Asian marine heatwaves. *Environ. Res. Lett.* **15**, 074008 (2020).
- Pak, G., Noh, J., Park, Y.-G., Jin, H. & Park, J.-H. Governing factors of the record-breaking marine heatwave over the mid-latitude western North Pacific in the summer of 2021. *Front. Marine Sci.* **9**, <https://doi.org/10.3389/fmars.2022.946767> (2022).
- Delworth, T. L. et al. SPEAR: The next generation GFDL modeling system for seasonal to multidecadal prediction and projection. *J. Adv. Model. Earth Syst.* **12**, <https://doi.org/10.1029/2019ms001895> (2020).
- Bretherton, C. S., Smith, C. & Wallace, J. M. An intercomparison of methods for finding coupled patterns in climate data. *J. Clim.* **5**, 541–560 (1992).
- Xu, M. et al. Distinct tropospheric and stratospheric mechanisms linking historical Barents-Kara sea-ice loss and late winter Eurasian temperature variability. *Geophys. Res. Lett.* **48**, e2021GL095262 (2021).
- Xu, M., Tian, W., Zhang, J., Wang, T. & Qie, K. Impact of sea ice reduction in the Barents and Kara Seas on the variation of the East Asian trough in late winter. *J. Clim.* **34**, 1081–1097 (2021).

22. Zhang, R. & Delworth, T. L. Impact of the Atlantic Multidecadal Oscillation on North Pacific climate variability. *Geophys. Res. Lett.* **34**, <https://doi.org/10.1029/2007GL031601> (2007).
23. Saranya, J. S. & Nam, S. Subsurface evolution of three types of surface marine heatwaves over the East Sea (Japan Sea). *Prog. Oceanogr.* **222**, 103226 (2024).
24. Reynolds, R. W. et al. Daily high-resolution-blended analyses for sea surface temperature. *J. Clim.* **20**, 5473–5496 (2007).
25. Hersbach, H. et al. The ERA5 global reanalysis. *Q. J. R. Meteorol. Soc.* **146**, 1999–2049 (2020).
26. Kirtman, B. P. et al. The North American Multimodel Ensemble: Phase-1 Seasonal-to-Interannual Prediction; Phase-2 toward Developing Intraseasonal Prediction. *Bull. Am. Meteorol. Soc.* **95**, 585–601 (2014).
27. Lu, F. et al. GFDL's SPEAR Seasonal Prediction System: Initialization and Ocean Tendency Adjustment (OTA) for Coupled Model Predictions. *J. Adv. Mod. Ear. Sys.* **12**, <https://doi.org/10.1029/2020ms002149> (2020).
28. Sun, C. et al. The Data Management System for the Global Temperature and Salinity Profile Programme in Proceedings of OceanObs.09: Sustained Ocean Observations and Information for Society, Vol. 2 (eds Hall, J., Harrison, D.E., & Stammer, D.) WPP-306, <https://doi.org/10.5270/OceanObs09.cwp.86> (ESA Publication, 2010).
29. Akazawa F. et al. Argo float data and metadata from Global Data Assembly Centre (Argo GDAC). *SEANOE* <https://www.seanoe.org/data/00311/42182/> (2019).
30. Saha, S. et al. The NCEP climate forecast system version 2. *J. Clim.* **27**, 2185–2208 (2014).
31. Tseng, K.-C. et al. Are multiseasonal forecasts of atmospheric rivers possible? *Geophys. Res. Lett.* **48**, e2021GL094000 (2021).
32. Bushuk, M. et al. Seasonal prediction and predictability of regional antarctic sea ice. *J. Clim.* **34**, 6207–6233 (2021).
33. Bushuk, M. et al. Mechanisms of regional arctic sea ice predictability in two dynamical seasonal forecast systems. *J. Clim.* **35**, 4207–4231 (2022).
34. Zhang, G. et al. Seasonal predictability of baroclinic wave activity. *npj Clim. Atmos. Sci.* **4**, 50 (2021).
35. Joh, Y. et al. Seasonal-to-decadal variability and prediction of the Kuroshio Extension in the GFDL Coupled Ensemble Reanalysis and Forecasting system. *J. Clim.* 1–59, <https://doi.org/10.1175/jcli-d-21-0471.1> (2022).
36. Yang, X. et al. On the seasonal prediction and predictability of winter surface Temperature Swing Index over North America. *Front. Clim.* **4**, <https://doi.org/10.3389/fclim.2022.972119> (2022).
37. Jia, L. et al. Skillful seasonal prediction of North American summertime heat extremes. *J. Clim.* **35**, 4331–4345 (2022).
38. Jia, L. et al. Seasonal prediction of North American wintertime cold extremes in the GFDL SPEAR forecast system. *Clim. Dyn.* **61**, 1769–1781 (2023).
39. Wallace, J. M., Smith, C. A. & Bretherton, C. S. Singular value decomposition of wintertime sea surface temperature and 500-mb height anomalies. *J. Clim.* **5**, 561–576 (1992).
40. Bretherton, C. S., Widmann, M., Dymnikov, V. P., Wallace, J. M. & Bladé, I. The effective number of spatial degrees of freedom of a time-varying field. *J. Clim.* **12**, 1990–2009 (1999).
41. Pak, G. et al. Upper-ocean thermal variability controlled by ocean dynamics in the Kuroshio-Oyashio Extension region. *J. Geophys. Res. Oceans* **122**, 1154–1176 (2017).
42. Vijith, V. et al. Closing the sea surface mixed layer temperature budget from in situ observations alone: Operation Advection during BoBBLE. *Sci. Rep.* **10**, 7062 (2020).
43. Marin, M., Feng, M., Bindoff, N. L. & Phillips, H. E. Local drivers of extreme upper ocean marine heatwaves assessed using a global ocean circulation model. *Front. Clim.* **4**, 788390 (2022).
44. Kim, S.-B., Fukumori, I. & Lee, T. The closure of the ocean mixed layer temperature budget using level-coordinate model fields. *J. Atmos. Ocean. Technol.* **23**, 840–853 (2006).
45. Talley, L. D., Pickard, G. L., Emery, W. J., Swift J. H. *Chapter 7 - dynamical processes for descriptive ocean circulation, Descriptive physical oceanography* 6th edn, 187–221 (Academic Press, 2011).

Acknowledgements

We thank the Joint Project Agreements (JPA) Project of the National Oceanic and Atmospheric Administration (NOAA) and the Ministry of Oceans and Fisheries (MOF) for funding that supported the collaboration. Young-Gyu Park and Gyundo Pak were supported by Korea Institute of Ocean Science & Technology (KIOST) (Strengthening of Prediction Capabilities for Marine Changes and Future Projections of Ocean Climate around the Korean Peninsula, PEA0203) and MOF, Korea (Investigation and prediction system development of marine heatwave around the Korean Peninsula originated from the subarctic and western Pacific, 20190344). We are especially grateful to Mr. Dong-Soo Han from MOF Liaison Office and Dr. YounHo Lee and Mr. Taehee Lee from NOAA-KIOST Lab for supporting the collaborative research. We also thank Donghyuck Yoon and Nathaniel Johnson for their constructive comments on an earlier version of the manuscript. This article was prepared by Youngji Joh under award NA22OAR4050664d from the National Oceanic and Atmospheric Administration, U.S. Department of Commerce. The statements, findings, conclusions, and recommendations are those of the authors and do not necessarily reflect the views of the National Oceanic and Atmospheric Administration or the U.S. Department of Commerce.

Author contributions

Y.J., S.L., and Y.P. conceived the study. Y.J. conducted the model output analysis, plotted figures, and wrote the paper. T.L.D., G.P., L.J., W.F.C., C.M., Y.K., and H.L. contributed to interpreting the results and enhancing discussions and helped to improve the manuscript.

Competing interests

The authors declare no competing interests.

Additional information

Correspondence and requests for materials should be addressed to Youngji Joh.

Reprints and permissions information is available at <http://www.nature.com/reprints>

Publisher's note Springer Nature remains neutral with regard to jurisdictional claims in published maps and institutional affiliations.

Open Access This article is licensed under a Creative Commons Attribution-NonCommercial-NoDerivatives 4.0 International License, which permits any non-commercial use, sharing, distribution and reproduction in any medium or format, as long as you give appropriate credit to the original author(s) and the source, provide a link to the Creative Commons licence, and indicate if you modified the licensed material. You do not have permission under this licence to share adapted material derived from this article or parts of it. The images or other third party material in this article are included in the article's Creative Commons licence, unless indicated otherwise in a credit line to the material. If material is not included in the article's Creative Commons licence and your intended use is not permitted by statutory regulation or exceeds the permitted use, you will need to obtain permission directly from the copyright holder. To view a copy of this licence, visit <http://creativecommons.org/licenses/by-nc-nd/4.0/>.

© The Author(s) 2024